ARTICLE

Lanthanide-grafted hollow bipyridine-based Periodic Mesoporous Organosilicas as chemical sensors

Received 00th January 20xx,
Accepted 00th January 20xx

DOI: 10.1039/x0xx00000x

Wanlu Liu,[a b c] Chunhui Liu,[b c] Luca Pilia,[d] Hongliang Zhang,[e] Pascal Van Der Voort,[c] Anna M. Kaczmarek,[b] and Rik Van Deun*[a]

We have synthesized a co-condensed hollow ethane-bipyridine periodic mesoporous organosilica (HEt-bpy-PMO) as a host material to anchor lanthanides for the purpose of developing a multifunctional chemical sensor. The host material was grafted with lanthanide chloride salts or complexes. The luminescence properties of the developed series of hybrid materials were studied in detail in the solid-state and after dispersing in water. The Eu^{3+} or Tb^{3+} singly incorporated materials were investigated for their use as ion sensors, showing ions selectivity towards Cu^{2+}, Co^{2+} and Fe^{3+}. Additionally, the Eu^{3+} or Tb^{3+} incorporated materials showed obvious luminescence quenching behavior towards acetone compared to other organic solvents, indicating excellent acetone sensing selectivity.

1. Introduction

A lot of attention has recently been given to lanthanide materials as luminescent sensor materials, especially lanthanide Metal–Organic Frameworks (MOFs). In the meantime, Periodic Mesoporous Organosilicas (PMOs), a novel class of porous materials, are developing into novel sensing support matrices.[1-3] Periodic mesoporous organosilicas (PMOs) possess ordered structure, tunable pore size, tailorable surface properties, and high hydrothermal and mechanical stability.[4] Various functional organic moieties can be integrated into the organosilica framework or onto the surface of the pore walls.

A very interesting class of PMO materials are the bipyridine-based PMOs. Many reports have shown that bipyridine-based PMOs have very good chelating ability with *d*-metal ions such as Ru(II), Ir(III), Re(I), Mn(VI), Mo(VI), and Pt(II).[5-8] However, the research on the interaction with lanthanide ions is still scarce. In general, the 2,2'-bipyridine ligand has been very widely used as chelating ligand for developing metal complexes in coordination and supramolecular chemistry.[9-11] Although there have been several reports on the synthesis of PMOs containing the 2,2'-bipyridine ligands, up until the report by Waki et al., these groups were randomly distributed on the pore surface or in the walls.[12-14] A novel bipyridine-PMO (bpy-PMO) was successfully synthesized from 100% organosilane precursor $[(i\text{-}PrO)_3Si\text{-}C_{10}H_6N_2\text{-}Si(Oi\text{-}Pr)_3]$.[15] This bpy-PMO had a crystal-like pore wall structure in which bipyridine moieties were densely and regularly arranged, preserving their high coordination ability to metals. Subsequently, two new co-condensed bipyridine-based PMOs were reported by Kaczmarek et al.[16] The materials were prepared by co-condensation of bipyridine-bridged alkoxysilane precursor and biphenyl- (bpy-bp-PMO) or ethane-bridged (bpy-Et-PMO) alkoxysilane precursors. Kaczmarek et al. also investigated the luminescence performance of these PMOs (bpy-PMO, bpy-bp-PMO and bpy-Et-PMO) grafted with lanthanide metal salts and lanthanide β-diketonate complexes.[16] They developed several different thermometric sensor systems based on Tb^{3+}, Dy^{3+}, Sm^{3+}. These bipyridine-based PMOs additionally showed no toxicity to human fibroblasts and were proposed as biological thermometers.

Recently, reports on hollow PMO structures have been attracting great interests.[17-19] Hollow structures are a major type of advanced materials that possess unique features, including low density, accommodated cavity, and functional walls. They have been adopted as spatially confined reactors for a broad range of applications.[20] Silica hard templating methods were wildly employed to synthesize hollow PMOs by researchers, which requires the etching of the silica core by using aqueous Na_2CO_3 or NaOH.[21,22] Kaczmarek et al. proposed a hollow bpy-Et-PMO as the host material to simultaneously anchor lanthanides and a vanadium oxodiperoxo complex for obtaining a multifunctional new material as a simultaneous heterogeneous catalyst and thermometer to monitor temperature in situ during an ongoing reaction.[23]

[a] *L^3 – Luminescent Lanthanide Lab, Department of Chemistry, Ghent University, Krijgslaan 281-S3, 9000 Ghent, Belgium.*
[b] *NanoSensing Group, Department of Chemistry, Ghent University, Krijgslaan 281-S3, 9000 Ghent, Belgium.*
[c] *Center for Ordered Materials, Organometallics and Catalysis (COMOC), Department of Chemistry, Ghent University, Krijgslaan 281-S3, 9000 Ghent, Belgium.*
[d] *Department of Mechanical, Chemical and Materials Engineering, University of Cagliari, Via Marengo 2, 09123 Cagliari, Italy.*
[e] *Shenzhen University General Hospital, Shenzhen University, Shenzhen 518060, P.R. China.*

†Electronic Supplementary Information (ESI) available: [details of any supplementary information available should be included here]. See DOI: 10.1039/x0xx00000x

Up to date, research towards chemical sensing properties of lanthanide-grafted bipyridine-based PMOs is quite scarce, especially in metal ion and organic solvent sensing. Herein, we report a silica hard templating method for the successful synthesis of hollow bipyridine-based PMOs by co-condensation of a bipyridine-bridged alkoxysilane precursor and 1,2-bis(triethoxysilyl)ethane. Considering the excellent binding ability of bipyridine moieties, the obtained hollow bipyridine PMOs were further grafted with lanthanide chloride ($LnCl_3$, Ln = Eu, Tb) or using 1,10-phenanthroline (phen) as the second co-ligand or grafted with lanthanide complexes ($Ln(tfac)_3$, tfac = 1,1,1-trifluoro-2,4-pentanedione). The final lanthanide-grafted PMO materials were investigated for their response to different metal ions (Fe^{3+}, Hg^{2+}, Pb^{2+}, Co^{2+} Cd^{2+}, Ca^{2+}, Zn^{2+}, Cu^{2+}, Cr^{3+}) at a 1000 ppm concentration. On the other hand, with the purpose of investigating potential applications of these lanthanide PMOs as solvent sensors, eight solvents (water, methanol, ethanol, isopropanol, n-butanol, acetone, DMSO, DMF) were chosen to study the sensor performance. Interestingly, we observed that all the studied hybrid PMO materials showed selective "turn off" fluorescence for acetone.

2. Experimental section

All starting materials were obtained from commercial suppliers and used directly without further purification: cetyltrimethylammonium bromide (CTAB, Acros Organics, 99+%), 1,1,1-trifluoro-2,4-pentanedione (Sigma-Aldrich, 98%), bis(triethoxysilyl)ethane (ABCR, 97%) and 5,5'-bis(triisopropoxysilyl)-2,2'-bipyridine (TCI, 95+%).

2.1 Synthesis of $Ln(tfac)_3$ complex

$Ln(tfac)_3$ complexes were synthesized according to a modified literature procedure.[24] 0.4 mL of 1,1,1-trifluoro-2,4-pentanedione was first added to ammonia solution (0.25 mL 25% ammonia solution with 2.5 mL distilled water) to form a wet solid. After stirring for a few seconds, 30 mL distilled water was added to the above to obtain a ligand solution. The ligand solution was then added slowly to the lanthanide chloride aqueous solution (1.08 mmol lanthanide chloride was dissolved in 5 mL distilled water) and stirred for 24 h. The precipitate was obtained by filtration, followed by drying for a few hours in air.

2.2 Synthesis of hollow Et-bpy-PMO (HEt-bpy-PMO)

This material was synthesized in three steps. SiO_2 particle cores were first grown and then a PMO shell was grown around them to form core-shell PMO particles. As the last step, the inner SiO_2 core was etched, which yielded hollow PMO particles.

The SiO_2 particle cores were prepared according to a published method.[21] 134 mL ethanol, 1.7 mL distilled water, and 15 mL 25% ammonia solution were mixed and magnetically stirred at 30 °C. Next, 6 mL tetraethyl orthosilicate (TEOS) was quickly added and the mixture was stirred overnight. The SiO_2 particles were kept in suspension without further purification. The next day, 50 mL of the above SiO_2 particles suspension was taken and diluted with 100 mL distilled water.

Core-shell SiO_2@Et-bpy-PMO particles were prepared by mixing 0.6 g cetyltrimethylammonium bromide (CTAB), 10 mL distilled water, and 5 mL ethanol in a flask.[21] The mixture was stirred for 30 min until CTAB was completely dissolved. In a following step, the suspension of SiO_2 core particles was added and left to stir for 30 min. Next, a solution of 1,2-bis(triethoxysilyl)ethane (985 mg) and 5,5'-bis(triisopropoxysilyl)-2,2'-bipyridine (672 mg, bpy precursor) in 1 mL ethanol was directly added and stirred overnight at room temperature. The product was collected by centrifugation and washed several times with distilled water and ethanol before drying at 80 °C in air.

Hollow Et-bpy-PMO particles were obtained by etching the SiO_2 core. 0.1 g core-shell SiO_2@Et-bpy-PMO particles was mixed with 0.636 g Na_2CO_3 in 20 mL distilled water in a flask. The mixture was heated to 80 °C and left to stir for 1 h. Afterwards, the particles were centrifuged and washed several times with distilled water and dried at 80 °C in air. Finally, three solvent extractions were carried out on the hollow Et-bpy-PMO particles to ensure full removal of the surfactant template. In each extraction, the as-synthesized material (ca. 1 g) was stirred into a solution which contains 200 mL of ethanol and 1 mL of concentrated hydrochloric acid at 80 °C for 6 h. Afterwards, the product was centrifuged and washed with both distilled water and ethanol before drying.

2.3 Synthesis of HEt-bpy-PMO@Ln

The HEt-bpy-PMO@Ln samples were prepared using a heating block. 0.006 g of HEt-bpy-PMO and 0.05 mmol of $LnCl_3 \bullet 6H_2O$ or $Ln(tfac)_3 \bullet 2H_2O$ (Ln = Eu, Tb) were placed in a Pyrex tube and 5 ml ethanol was added. The tube was placed in the ultrasound bath for 10 min, and next heated on a heating block for 24 h at 80 °C. Afterwards, the mixture was cooled down to the room temperature, centrifuged and washed three times with ethanol. It was dried in an oven at 80 °C. HEt-bpy-PMO@Ln_phen was prepared in a similar way, except that 0.05 mmol of phenanthroline was added to the solution.

2.4 Characterization

Powder X-ray diffraction (PXRD) patterns were recorded using a Bruker D8 Advance diffractometer equipped with a Cu Kα (λ = 1.5405 Å) source in a 2θ range from 1° to 8° with a step size of 0.02°. Nitrogen adsorption-desorption isotherms were measured by using a Micromeritics TriStar 3000 analyzer at -196 °C. The samples were vacuum dried for 24 h at 120 °C before the measurements. The specific surface area (S_{BET}) was calculated using the Brunauer–Emmett–Teller (BET) method. Thermo-gravimetric analysis (TGA) was carried out on an SDT Q600 analyser in the temperature range of 50-800 °C under air flow at a heating rate of 10 °C min^{-1}. Transmission Electron Microscopy (TEM) images were obtained using a Cs-corrected JEOL JEM2200FS transmission electron microscope with a working voltage of 200 kV. Scanning TEM (STEM) images were taken with a high-angle annular dark field (HAADF) detector.

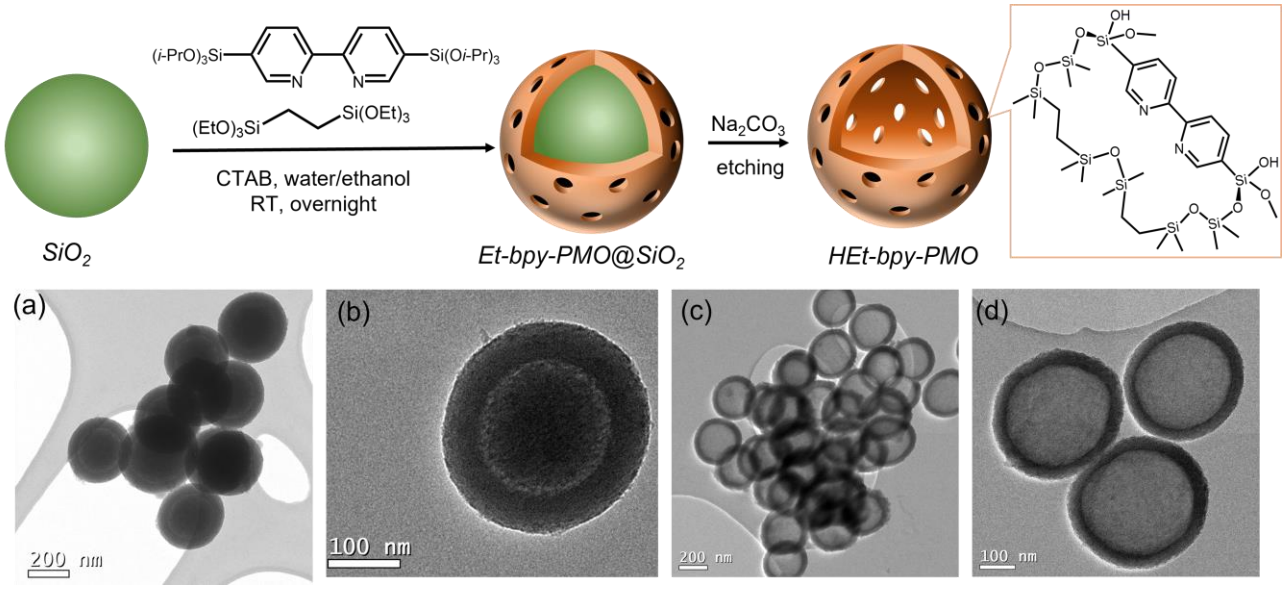

Figure 1 Schematic synthesis of HEt-bpy-PMO and TEM images of (a, b) Et-bpy-PMO@SiO_2 before etching and (c,d) HEt-bpy-PMO obtained by an etching process.

The composition of the sample was determined via energy dispersive X-ray (EDX) spectroscopy in HAADF-STEM mode. Elemental analysis (CHNS) was performed on a Thermo Flash 2000 elemental analyzer by using V_2O_5 as catalyst. UV–vis absorption spectra were recorded with a Perkin Elmer Lambda 950 spectrometer. The luminescence excitation and emission spectra were recorded using an Edinburgh Instruments FLSP920 UV-vis-NIR spectrometer setup with a 450 W xenon lamp as the steady state excitation source. The emission signals were detected using a Hamamatsu R928P photomultiplier tube. All emission spectra have been corrected for detector response. Luminescence decay times were recorded using a 60 W pulsed xenon lamp, operating at a frequency of 100 Hz. Small amounts of solid samples were placed between quartz plates (Starna cuvettes for powdered samples, type 20/C/Q/0.2) when measuring the luminescence properties. Colloidal suspensions of the PMO were measured in quartz cuvettes with a path length of 10 mm.

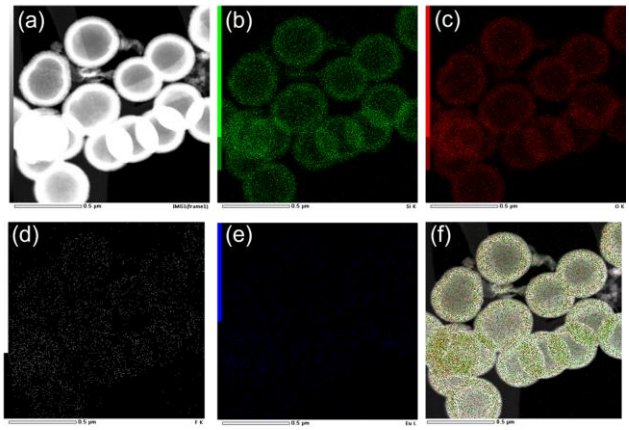

Figure 2 HAADF-STEM image of HEt-bpy-PMO@Eu(tfac)$_3$ (a) together with the corresponding element distributions obtained by EDX spectroscopy analysis for silicon (b), oxygen (c), fluorine (d), europium (e) and overlay (f).

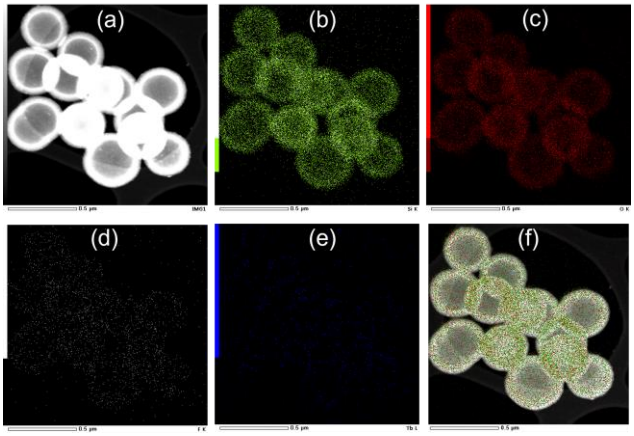

Figure 3 HAADF-STEM image of HEt-bpy-PMO@Tb(tfac)$_3$ (a) together with the corresponding element distributions obtained by EDX spectroscopy analysis for silicon (b), oxygen (c), fluorine (d), terbium (e) and overlay (f).

3. Results and discussion

3.1 Characterization of HEt-bpy-PMO and HEt-bpy-PMO@Ln

A schematic overview of the synthesis procedure for HEt-bpy-PMO is given in Figure 1. The bipyridine group content in HEt-bpy-PMO was found to be 1.61 mmol g^{-1} by CHNS elemental analysis. The morphology of the Et-bpy-PMO@SiO_2 (before etching out the SiO_2 template) and HEt-bpy-PMO (after etching out the SiO_2 template) was investigated in detail, as shown in Figure 1(a-d). A clear distinction between the SiO_2 core and the PMO shell can be observed in Figure 1(a) and (b). The Et-bpy-PMO@SiO_2 particles show uniform spheres with the average particle size of 320 nm (Figure S1). The PMO shell is around 52 nm in thickness. After the etching procedure, a hollow void was obtained due to the removal of SiO_2 core, as shown in Figure 1(c) and 1(d)). It was apparently that the shell thickness

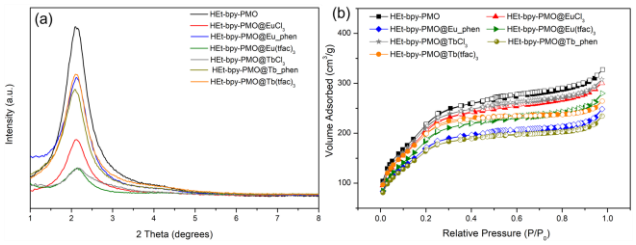

Figure 4 Powder XRD patterns (a) and N_2 adsorption-desorption isotherms (b) for HEt-bpy-PMO, HEt-bpy-PMO@$LnCl_3$, HEt-bpy-PMO@Ln_phen and HEt-bpy-PMO@Ln$(tfac)_3$ (Ln = Eu, Tb).

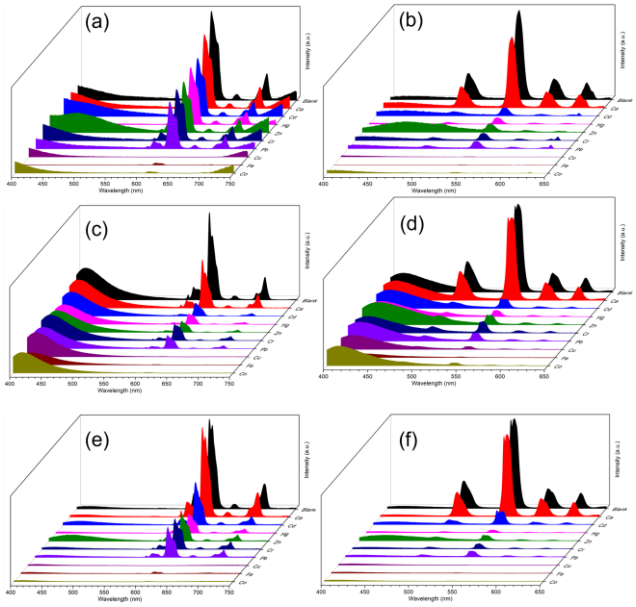

Figure 5 Luminescence spectra of HEt-bpy-PMO@Ln^{3+} colloidal suspensions (1 mg/1mL) in the presence of different metal ions: (a) HEt-bpy-PMO@$EuCl_3$ (excited at 310 nm), (b) HEt-bpy-PMO@$TbCl_3$ (excited at 312 nm), (c) HEt-bpy-PMO@Eu_phen (excited at 310 nm), (d) HEt-bpy-PMO@Tb_phen (excited at 310 nm), (e) HEt-bpy-PMO@Eu$(tfac)_3$ (excited at 309 nm), and (f) HEt-bpy-PMO@Tb$(tfac)_3$ (excited at 313 nm).

of the PMO had decreased to 40 nm (Figure S1). Upon grafting lanthanide chlorides or complexes to HEt-bpy-PMO, no change in morphology is observed (Figure 2 and 3). HAADF-STEM with EDX maps was carried out on both HEt-bpy-PMO@Eu$(tfac)_3$ and HEt-bpy-PMO@Tb$(tfac)_3$ (Figure 2 and 3) and showed the presence of lanthanide complexes on the PMO shell.

The powder X-ray diffraction patterns of HEt-bpy-PMO, HEt-bpy-PMO@$LnCl_3$, HEt-bpy-PMO@Ln$(tfac)_3$ and HEt-bpy-PMO@Ln_phen (Ln = Eu, Tb) are presented in Figure 4(a). A strong diffraction peak corresponding to the (100) reflections at around 2.11° is clearly observed for the HEt-bpy-PMO material, which is typical for a material with a mesoporous structure. No peaks were observed at medium angles (5° < 2θ < 40°), indicating an amorphous pore wall structure where the bipyridine groups were randomly embedded in the pores.[16] After grafting the lanthanides to HEt-bpy-PMO, the intensity of reflection (100) decreases for all HEt-bpy-PMO@Ln materials, mostly due to the addition of heavy metals.[25]

The N_2 sorption isotherms for these PMO samples are shown in Figure 4(b). All materials exhibit the typical type IV isotherms for mesoporous materials according to the IUPAC classification, suggesting the formation of a uniform mesoporous structure. The BET surface areas and other physical properties of all PMO materials are summarized in Table S1. The pristine HEt-bpy-PMO material has high BET surface area of 848 m^2g^{-1}. The BET surface areas of HEt-bpy-PMO@Ln materials decreased due to the introduction of the lanthanides into the PMO framework.

We also studied the thermal stability of HEt-bpy-PMO@Ln materials by thermogravimetric analysis (TGA). As examples, HEt-bpy-PMO@$LnCl_3$ (Ln =Eu, Tb) were selected and their TGA profiles are shown in Figure S2. Both materials are thermally stable up to approximately 400 °C, and gradually decompose at higher temperature.

3.2 Metal ion sensing selectivity of HEt-bpy-PMO@Ln

The room temperature photoluminescence excitation and emission spectra of the pristine HEt-bpy-PMO were recorded and have been presented in Figure S3. The excitation spectrum consists of a broad band between 300 and 400 nm, with a maximum at 365 nm. In the emission spectrum a broad band between 400 and 600 nm is observed with a maximum at 430 nm. Room temperature photoluminescence measurements were also carried out for all six lanthanide-grafted HEt-bpy-PMO materials, HEt-bpy-PMO@$LnCl_3$, HEt-bpy-PMO@Ln_phen and HEt-bpy-PMO@ Ln$(tfac)_3$ (Ln = Eu, Tb), both in the solid state as well as in the form of an aqueous colloidal suspension. The combined excitation-emission spectra of all materials have been presented in Figures S4-S9. All prepared solid-state Eu^{3+} and Tb^{3+} samples showed strong visible emission when placed under a UV lamp with an excitation wavelength of 302 nm (the insets of Figures S4-S9). The peak assignment of the labelled peaks for the solid-state samples has been done in Tables S2-S7. The characteristic emission peaks of Eu^{3+} and Tb^{3+} are found in the samples. In all the cases, a broad ligand band in the excitation spectra is observed. The maximum of this band slightly decreases in the colloidal suspensions compared to that in the solid state (Table S8). The luminescence decay profiles of all the samples in the solid-state and suspensions are given in Figures S10-S15. In almost all cases a good fit could only be obtained using a biexponential function. In the case of HEt-bpy-PMO@$EuCl_3$, HEt-bpy-PMO@$TbCl_3$, HEt-bpy-PMO@Eu$(tfac)_3$ and HEt-bpy-PMO@Tb$(tfac)_3$, we observe a decrease in the decay time when the samples are in the suspension compared to that of the solid-state samples (Table S9), most likely due to the quenching effect caused by water molecules.[4] However, for HEt-bpy-PMO@Eu_phen and HEt-bpy-PMO@Tb_phen samples, an increase of the luminescence decay times can be observed when dispersing the samples in water solution (Table S9).

To explore selective metal ion sensing by these hybrid materials, the as-synthesized samples were added into different standard nitrate solutions containing 1000 ppm metal nitrate salts (Ca^{2+}, Cd^{2+}, Hg^{2+}, Zn^{2+}, Cr^{3+}, Pb^{2+}, Cu^{2+}, Fe^{3+}, Co^{2+}). The colloidal suspensions were obtained by treating the samples (1 mg) in the nitrate solutions (1 mL) with ultrasound irradiation for 15 minutes until they formed very stable colloidal suspensions. The emission spectra of the

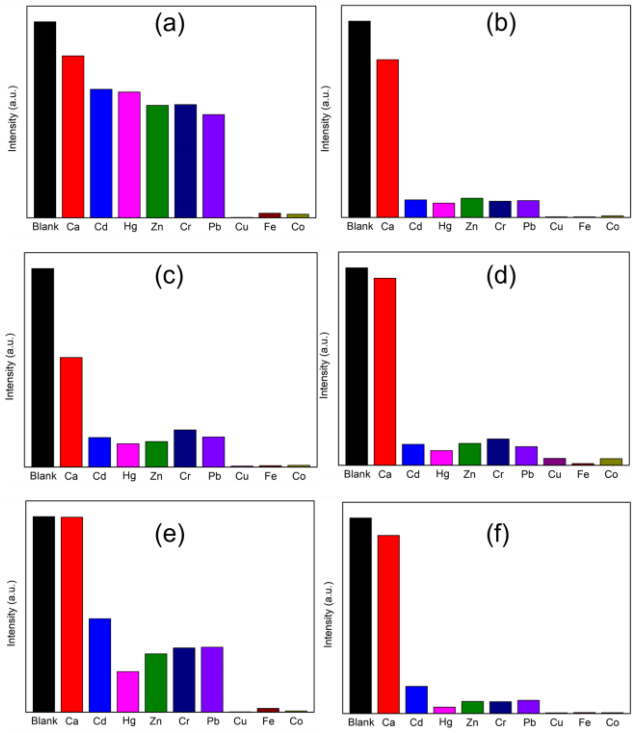

Figure 6 Luminescence intensity of the $^5D_0 \rightarrow {}^7F_2$ transition peak of HEt-bpy-PMO@Eu^{3+} samples and the $^5D_4 \rightarrow {}^7F_5$ transition peak of HEt-bpy-PMO@Tb^{3+} samples in the presence of different metal ions compared to the blank sample: (a) HEt-bpy-PMO@$EuCl_3$, (b) HEt-bpy-PMO@$TbCl_3$, (c) HEt-bpy-PMO@Eu_phen, (d) HEt-bpy-PMO@Tb_phen, (e) HEt-bpy-PMO@Eu(tfac)$_3$, and (f) HEt-bpy-PMO@Tb(tfac)$_3$.

HEt-bpy-PMO@$EuCl_3$, HEt-bpy-PMO@$TbCl_3$, HEt-bpy-PMO@Eu_phen, HEt-bpy-PMO@Tb_phen, HEt-bpy-PMO@Eu(tfac)$_3$ and HEt-bpy-PMO@Tb(tfac)$_3$ suspensions in the presence of different metal ions are shown in Figure 5. In Figure 6 we also compared the emission intensities of the samples in different metal ion solutions compared to the blank suspension (luminescence intensities recorded for the strongest peaks: $^5D_0 \rightarrow {}^7F_2$ for Eu^{3+} samples and $^5D_4 \rightarrow {}^7F_5$ for Tb^{3+} samples). Here, all the metal ions have a quenching effect on the emission intensity of the HEt-bpy-PMO@Ln suspensions compared to the blank suspension. Cu^{2+}, Co^{2+} and Fe^{3+} ions show more intense quenching behavior compared to other metal ions (Ca^{2+}, Cd^{2+}, Hg^{2+}, Zn^{2+}, Cr^{3+} and Pb^{2+}). It is worth noting that the Eu^{3+} and Tb^{3+} samples show similar behavior, suggesting that the metal ion sensing behavior is not lanthanide dependent (at least for lanthanide ions with similar ionic radius such as the investigated Eu^{3+} and Tb^{3+}). This sensing behavior was also reported by Kaczmarek et al.[26] Introducing an additional phen ligand or Eu(tfac)$_3$ complex causes a more pronounced quenching effect on the emission intensity of both HEt-bpy-PMO@Eu_phen and HEt-bpy-PMO@Eu(tfac)$_3$ suspensions in the presence of Cd^{2+}, Hg^{2+}, Zn^{2+}, Cr^{3+} and Pb^{2+}, compared to that of HEt-bpy-PMO@$EuCl_3$. However, for Tb^{3+} samples, no significant change on the quenching effect can be observed when introducing an additional phen ligand or Eu(tfac)$_3$ complex.

The above results of the metal ion sensing show that these lanthanides grafted bipyridine based PMOs are more ion

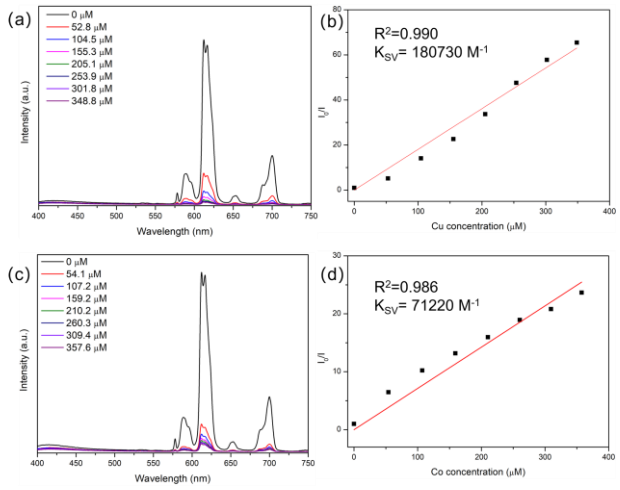

Figure 7 Luminescence spectra of a colloidal suspension of HEt-bpy-PMO@Eu(tfac)$_3$ treated with different concentrations of (a) Cu^{2+} and (c) Co^{2+}. Stern-Volmer plots of HEt-bpy-PMO@Eu(tfac)$_3$ for various concentrations of (b) Cu^{2+} and (d) Co^{2+}.

selective towards these three metal ions, Cu^{2+}, Co^{2+} and Fe^{3+}. The possible reasons for the "turn off" luminescence behavior are complex. It is known that some d-block element ions, such as Mn^{2+}, Co^{2+} and Cu^{2+}, have unsaturated *d* electronic configurations, which enable them to accept energy from lanthanide ions through *d-d* electron transitions, resulting in the quenching of lanthanide luminescence through $f \rightarrow d$ energy transfer.[4, 27] In another study, it has been reported that the selectivity of Eu-MOFs for Fe^{3+} ions most likely originated from the synergistic effect of competitive absorption and the strong electrostatic interactions between Fe^{3+} ions and the pyridine N atoms in the Eu-MOFs.[28]

In general, a number of processes can lead to a reduction of the luminescence intensity, so called quenching. Quenching can occur during the excited state lifetime (such as collisional quenching, energy transfer or charge transfer reaction) or it can occur in the ground state due to the formation of complexes.[26, 29] There are two common quenching process, dynamic quenching and static quenching. Dynamic quenching originates from the collision between the excited fluorophore and a quencher that can facilitate non-radiative transitions to the ground state. Static quenching occurs when a nonfluorescent ground-state complex is formed through the interaction between fluorophore and quencher. To better understand the quenching mechanism of ion sensing behavior in our systems, further studies were carried out on the sensing properties of HEt-bpy-PMO@Eu(tfac)$_3$ towards Cu^{2+} and Co^{2+} ions. As both Eu^{3+} and Tb^{3+} samples showed similar sensing behavior only one system was studied. Based on the emission intensity change with the addition of the metal ions at different concentrations (Figure 7(a), 7(c) and Figure S16), the luminescence quenching efficiency (K_{sv}) was analyzed using the Stern-Volmer (S-V) equation, $I_0/I = K_{sv}\,c+1$ (I and I_0 are the luminescence intensity of a colloidal suspension of HEt-bpy-PMO@Eu(tfac)$_3$ in the presence and absence of the metal ion, and *c* is the concentration of the metal ion). In Figure 7(b), 7(d) the responses of HEt-bpy-PMO@Eu(tfac)$_3$ to the addition of different concentration of Cu^{2+} and Co^{2+} are plotted along with

the S–V curves. The plots for Cu^{2+} and Co^{2+} could be fitted with a straight line, with very good fits around $R^2 = 0.98$. From the slope we calculated the K_{sv} values, which were determined to be 180730 M^{-1} for Cu^{2+}, 71220 M^{-1} for Co^{2+}, respectively. Based on the above results we also determined the limit of detection (LOD), supposing that LOD = $3\sigma/K_{SV}$, where σ is the standard deviation.[26] The LOD was calculated to be 0.19 μM for Cu^{2+}, 0.52 μM for Co^{2+}, respectively. A comparison with other reported PMO materials that have been used as metal ion (Cu^{2+} or Co^{2+}) sensors is shown in Table S10.

Possible quenching mechanisms for the luminescence responses to Cu^{2+} and Co^{2+} are further discussed. The I_0/I versus *c* plots are all linear for the whole range of quencher concentration. Therefore, the luminescence quenching can be attributed either to being purely dynamic, or purely static. On the contrary, if both static and dynamic quenching were occurring in the sample than the I_0/I versus *c* plot should have an upward curvation.[4] This is obviously not the case in our systems, in which a good linear fit can be found. Luminescence lifetime measurements were carried out to further evaluate the nature of the quenching process. As depicted in Figure S17 (a) and (b), we can observe a slight drop in the decay times when increasing concentrations of Cu^{2+} as well as Co^{2+}, indicating that the quenching is dynamic in both cases. We have also performed anti-interference tests for HEt-bpy-PMO@Eu(tfac)$_3$, and the results are shown in Figure S18. The luminescence intensity shows a significant decrease in the coexistence of a quenching ion (e.g., Ca^{2+}, Cd^{2+}, Hg^{2+}…) and Cu^{2+} or Co^{2+} compared to the intensity of the quenching ion. Therefore, even in a mixed solution where other ions are present, the presence of Cu^{2+} or Co^{2+} can be detected based on the weaker emission intensity of the solutions. Additionally, the structural stability of HEt-bpy-PMO@Ln after metal ion sensing experiments was determined by PXRD, taking HEt-bpy-PMO@TbCl$_3$ as an example, as shown in Figure S19. The mesoporous structure is still maintained after sensing experiments, indicating the structural stability for HEt-bpy-PMO@TbCl$_3$.

3.3 Organic solvent sensing selectivity of HEt-bpy-PMO@Ln

In this part of our study, all prepared HEt-bpy-PMO@LnCl$_3$, HEt-bpy-PMO@Ln_phen and HEt-bpy-PMO@Ln(tfac)$_3$ (Ln = Eu, Tb) materials were further studied for their optical response in the presence of various solvents (water, methanol, ethanol, isopropanol, n-butanol, acetone, DMSO, and DMF). For the solvent sensing tests 1 mg of sample was dispersed in 1 mL of each of the studied solvents, with ultrasound irradiation for a few minutes to form a stable suspension. As shown in Figure 8(a) and (b), we can observe a significant decrease in the luminescence intensity for HEt-bpy-PMO@EuCl$_3$ when dispersed in acetone compared to the water suspension, while different degrees of enhancement in luminescence intensities are seen in other solvents. Similar behavior can also be found both in HEt-bpy-PMO@Eu_phen and HEt-bpy-PMO@Eu(tfac)$_3$ suspensions (Figure 8(c)-(f)). As for the Tb^{3+} samples, the luminescence intensities of all studied Tb^{3+} samples show the most intense quenching effect in acetone suspension

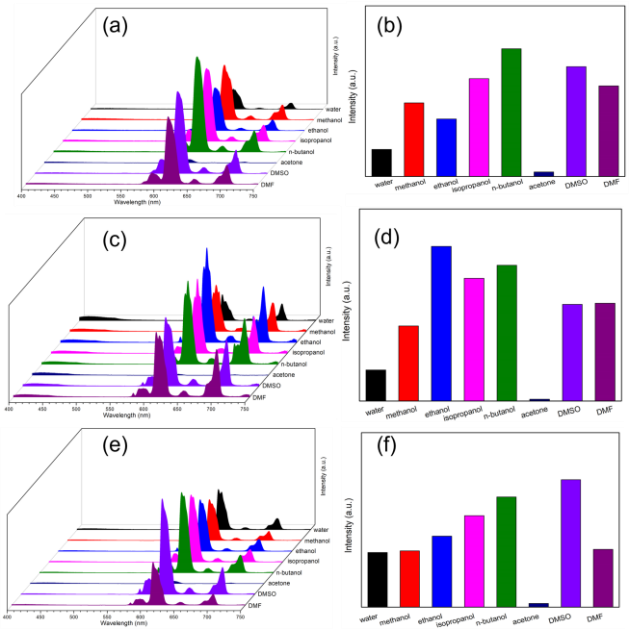

Figure 8 (a) Luminescence spectra of HEt-bpy-PMO@EuCl$_3$ dispersed in different solvents, (b) luminescence intensity of the $^5D_0 \rightarrow {}^7F_2$ transition of HEt-bpy-PMO@EuCl$_3$ dispersed in different solvents, (c) luminescence spectra of HEt-bpy-PMO@ Eu_phen dispersed in different solvents, (d) luminescence intensity of the $^5D_0 \rightarrow {}^7F_2$ transition of HEt-bpy-PMO@ Eu_phen dispersed in different solvents, (e) luminescence spectra of HEt-bpy-PMO@ Eu(tfac)$_3$ dispersed in different solvents, and (f) luminescence intensity of the $^5D_0 \rightarrow {}^7F_2$ transition of HEt-bpy-PMO@ Eu(tfac)$_3$ dispersed in different solvents.

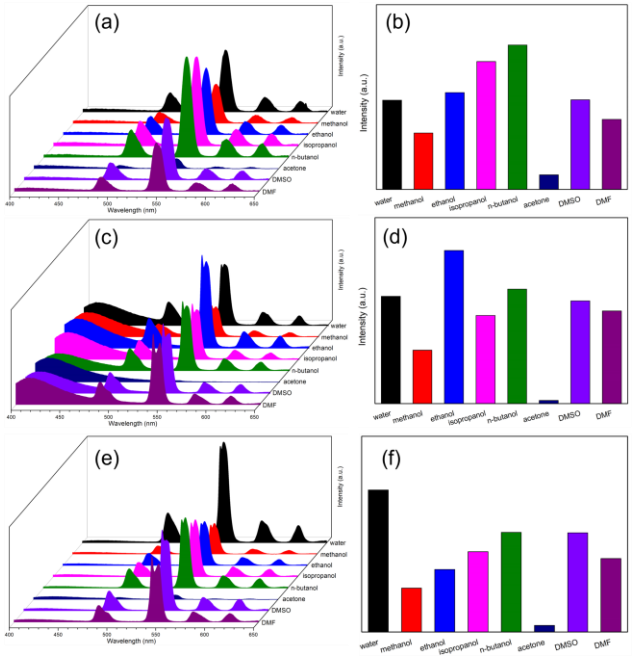

Figure 9 (a) Luminescence spectra of HEt-bpy-PMO@TbCl$_3$ dispersed in different solvents, (b) luminescence intensity of the $^5D_4 \rightarrow {}^7F_5$ transition of HEt-bpy-PMO@TbCl$_3$ dispersed in different solvents, (c) luminescence spectra of HEt-bpy-PMO@Tb_phen dispersed in different solvents, (d) luminescence intensity of the $^5D_4 \rightarrow {}^7F_5$ transition of HEt-bpy-PMO@Tb_phen dispersed in different solvents, (e) luminescence spectra of HEt-bpy-PMO@Tb(tfac)$_3$ dispersed in different solvents, and (f) luminescence intensity of the $^5D_4 \rightarrow {}^7F_5$ transition of HEt-bpy-PMO@Tb(tfac)$_3$ dispersed in different solvents.

compared to the other studied organic solvents (Figure 9). Based on the above results, we proposed that

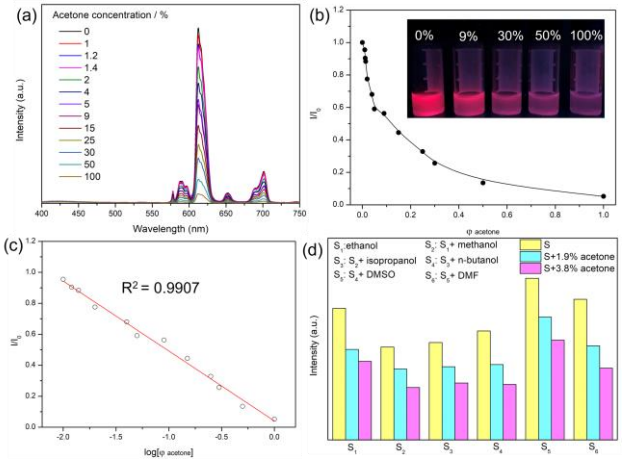

Figure 10 (a) Luminescence spectra of HEt-bpy-PMO@Eu(tfac)$_3$ as dispersions in mixed organic solvents (acetone / ethanol), (b) relationship between the I/I_0 and acetone volume (the inset is the photo taken under a UV lamp (302 nm excitation)), (c) relationship between the I/I_0 and the logarithm of acetone volume, and (d) luminescence intensities of the $^5D_0 \rightarrow {}^7F_2$ transition of HEt-bpy-PMO@ Eu(tfac)$_3$ present in multicomponent mixed solutions.

HEt-bpy-PMO@Ln^{3+} materials show a unique selectivity to acetone, suggesting that the solvent sensing behavior is also not lanthanide dependent, similar to the metal ion sensing behavior. Therefore, HEt-bpy-PMO@Ln^{3+} materials can be applied as "turn-off" luminescent sensors to detect acetone.

As an example, HEt-bpy-PMO@Eu(tfac)$_3$ was dispersed in ethanol as the standard suspension, while different volumes of acetone were added into ethanol dispersions for further investigation. Regular quenching upon adding different volumes of acetone into ethanol dispersions of HEt-bpy-PMO@Eu(tfac)$_3$ is shown in Figure 10(a). The luminescence intensity of HEt-bpy-PMO@Eu(tfac)$_3$ gradually decreased with the increase of acetone concentrations. A gradually weakened red luminescence can be observed when increasing the acetone concentration, as was also witnessed by the appearance of HEt-bpy-PMO@Eu(tfac)$_3$ dispersions when placed under a UV lamp (302 nm excitation; see Figure 10(b), inset). A typical Stern-Volmer plot for the luminescence quenching with acetone shows a downward curvature rather than linear behavior (Figure 10(b)), while a modified Stern–Volmer plot (Figure 10(c)) displays a linear correlation between the luminescence intensity and the concentration of acetone added. A linear correlation coefficient of 0.9907 is found over a very extensive acetone concentration range between 1% and 100% as presented in Figure 10(c). The Stern–Volmer quenching process applied here was based on a modified Stern–Volmer linear fit method.[30] Additionally, the luminescence quenching behavior of HEt-bpy-PMO@Tb(tfac)$_3$ was also investigated in different acetone/ethanol suspensions. A similar downward curvature of the Stern-Volmer plot and linear relationship on the modified Stern–Volmer plot of HEt-bpy-PMO@Tb(tfac)$_3$ can also be observed in Figure S20, compared to the quenching behavior of HEt-bpy-PMO@Eu(tfac)$_3$. In the meantime, we also investigated the luminescence quenching behavior of HEt-bpy-PMO@Ln(tfac)$_3$ (Ln = Eu, Tb) in acetone/water suspensions (Figure S21). A downward curvature of the Stern-Volmer plot were observed, for both HEt-bpy-PMO@Ln(tfac)$_3$ materials (Ln = Eu, Tb). Both HEt-bpy-PMO@Ln(tfac)$_3$ materials (Ln = Eu, Tb) exhibit a very high sensitivity towards acetone even at extremely low concentrations down to 1%, which is superior to other reported lanthanide porous materials (Table S11).

We also performed anti-interference tests for HEt-bpy-PMO@Eu(tfac)$_3$, as shown in Figure 10(d). The HEt-bpy-PMO@Eu(tfac)$_3$ sensor shows obvious luminescence quenching after the introduction of acetone to several solvents such as methanol, isopropanol, n-butanol, DMSO, DMF and ether as well as their combinations, indicating an excellent anti-interference property. The stability of both HEt-bpy-PMO@Eu(tfac)$_3$ and HEt-bpy-PMO@Tb(tfac)$_3$ materials as acetone sensors was also studied. As shown in Figure S22, there is no significant change in the PXRD patterns as well as the decay profiles of both PMO materials before and after acetone treatments. The former means the retention of the PMO framework, and the latter means the lanthanide ions did not come off the PMO. These results indicate good chemical stability of HEt-bpy-PMO@Eu(tfac)$_3$ and HEt-bpy-PMO@Tb(tfac)$_3$.

The mechanism of luminescence "turn off" behavior for the detection of acetone can be explained by the competitive absorption of the light source energy upon excitation between the solvents and HEt-bpy-PMO@Ln^{3+} (Ln = Eu, Tb). Distinguished from other solvents presenting no obvious UV-vis absorption, acetone exhibits a strong absorption ranging from 280 to 340 nm (Figure S23), which overlaps the UV-vis absorption of HEt-bpy-PMO@Ln^{3+} (Figure S24). This indicates that the luminescence quenching of HEt-bpy-PMO@Ln^{3+} by acetone was caused by the fluorescence resonance energy transfer (FRET). This suggests that in an emulsion the acetone will absorb most of the excitation energy and only a small fraction of the energy will be absorbed by the ligands. Hence, very little energy will be transferred through the ligands to the Ln^{3+} ions, resulting in an obvious decrease in luminescence intensity or even total luminescence quenching. Additionally, photoinduced electron transfer (PET) was also considered as a possible luminescence quenching mechanism. DFT calculations were performed to investigate the quenching mechanism of HEt-bpy-PMO@Ln^{3+} for acetone. The LUMO of the bpy ligand (-2.15 eV) was calculated to be lower than the LUMO of acetone (-0.83 eV), indicating that the bpy ligand cannot transfer excited electrons from the PMO framework to acetone. Therefore, according to above results, only the FRET process can be considered as the responsable quenching mechanism.

As chemical sensors, it is of great importance to ensure the stability of the materials in acidic and alkaline solutions. Taking HEt-bpy-PMO@Eu_phen as an example, the luminescence spectra and corresponding intensities of the material dispersed in solutions with different pH values are shown in Figure S25(a) and (b). The luminescence intensities almost had no significant change after 5 cycles of pH treatments (Figure S25 (c)). Further PXRD patterns confirmed the retention of the PMO framework after the pH treatments (Figure S25(d)),

which indicated the chemical stability of HEt-bpy-PMO@Eu_phen.

Conclusions

In this work, we have developed multifunctional chemical sensors, based on lanthanide incorporated hollow bipyridine-based PMOs, for sensing of Cu^{2+} and Co^{2+} metal ions, and acetone. These chemical sensors are prepared by grafting lanthanide chlorides, or lanthanide with phen ligand, or lanthanide complexes ($Ln(tfac)_3$, Ln = Eu, Tb) onto/into the HEt-bpy-PMO. Six Eu^{3+}, Tb^{3+} singly incorporated PMOs were synthesized and fully characterized. All six lanthanide singly incorporated PMOs showed similar metal ion sensing as well as solvent sensing behaviors, regardless of whether the incorporated lanthanide ions are Eu^{3+} or Tb^{3+}. On the other hand, it was observed that the presence or absence of the additional co-ligand phen had no significant effect on the chemical sensing and its selectivity. HEt-bpy-PMO@$Eu(tfac)_3$ (as a representative example) showed high detection ability to sense Cu^{2+} (LOD = 0.18 μM), or Co^{2+} (LOD = 0.61 μM) ions or acetone (LOD = 1%) via luminescence quenching.

Conflicts of interest

There are no conflicts to declare.

Acknowledgements

W. L. acknowledges financial support from the China Scholarship Council (CSC, No. 201804910742). A. M. K. thanks Ghent University (BOF Starting Grant) under award number [BOF/STA/202002/004] for financial support. The authors would like to thank Dr. Shinji Inagaki for valuable discussions concerning bipyridine PMO materials.

References

1 S. N. Zhao, G. Wang, D. Poelman and P. Van Der Voort, *Materials*, 2018, **11**.
2 W. P. Lustig, S. Mukherjee, N. D. Rudd, A. V. Desai, J. Li and S. K. Ghosh, *Chem. Soc. Rev.*, 2017, **46**, 3242-3285.
3 J. Y. Lei, L. G. Yang, D. L. Lu, X. F. Yan, C. Cheng, Y. D. Liu, L. Z. Wang and J. L. Zhang, *Adv. Opt. Mater.*, 2015, **3**, 57-63.
4 W. Liu, A. M. Kaczmarek, H. Rijckaert, P. Van Der Voort and R. Van Deun, *Dalton Trans.*, 2021, **50**, 11061-11070.
5 M. Waki, K. I. Yamanaka, S. Shirai, Y. Maegawa, Y. Goto, Y. Yamada and S. Inagaki, *Chem. Eur.J.*, 2018, **24**, 3846-3853.
6 S. Ishikawa, Y. Maegawa, M. Waki and S. Inagaki, *ACS Catal.*, 2018, **8**, 4160-4169.
7 X. Wang, I. Thiel, A. Fedorov, C. Coperet, V. Mougel and M. Fontecave, *Chem. Sci.*, 2017, **8**, 8204-8213.
8 H. Matsukawa, M. Yoshida, T. Tsunenari, S. Nozawa, A. Sato-Tomita, Y. Maegawa, S. Inagaki, A. Kobayashi and M. Kato, *Sci. Rep.*, 2019, **9**, 15151.
9 C. Kaes, A. Katz and M. W. Hosseini, *Chem. Rev.*, 2000, **100**, 3553−3590.
10 L. c. J. C. re, R. Ziessel, M. Montalti, L. Prodi, N. Zaccheroni, C. Boehme and G. Wipff, *J. Am. Chem. Soc.*, 2002, **124**, 7779-7788.
11 l. S. Schubert and C. Eschbaumer, *Angew. Chem. Int. Ed.* , 2002, **41**, 2892-2926.
12 L. Sun, W. Mai, S. Dang, Y. Qiu, W. Deng, L. Shi, W. Yan and H. Zhang, *J. Mater. Chem.*, 2012, **22**, 5121.
13 J. Font, P. de March, F. Busqué, E. Casas, M. Benitez, L. Teruel and H. García, *J. Mater. Chem.*, 2007, **17**, 2336-2343.
14 Y.-J. Li, L. Wang and B. Yan, *J. Mater. Chem.*, 2011, **21**, 1130-1138.
15 M. Waki, Y. Maegawa, K. Hara, Y. Goto, S. Shirai, Y. Yamada, N. Mizoshita, T. Tani, W. J. Chun, S. Muratsugu, M. Tada, A. Fukuoka and S. Inagaki, *J. Am. Chem. Soc.*, 2014, **136**, 4003-4011.
16 A. M. Kaczmarek, Y. Maegawa, A. Abalymov, A. G. Skirtach, S. Inagaki and P. Van Der Voort, *ACS Appl. Mater. Interfaces*, 2020, **12**, 13540-13550.
17 H. Djojoputro, X. F. Zhou, S. Z. Qiao, L. Z. Wang, C. Z. Yu and G. Q. Lu, *J. Am. Chem. Soc.*, 2006, **128**, 6320-6321.
18 N. Ma, Y. Deng, W. Liu, S. Li, J. Xu, Y. Qu, K. Gan, X. Sun and J. Yang, *Chem. Commun.*, 2016, **52**, 3544-3547.
19 J. Liu, S. Bai, H. Zhong, C. Li and Q. Yang, *J. Phys. Chem. C* 2010, **114**, 953–961.
20 D. Liu, J. Wan, G. Pang and Z. Tang, *Adv. Mater.*, 2019, **31**, 1803291.
21 A. M. Kaczmarek, M. Suta, H. Rijckaert, A. Abalymov, I. Van Driessche, A. G. Skirtach, A. Meijerink and P. Van Der Voort, *Adv. Funct. Mater.*, 2020, **30**, 2003101.
22 Y. Chen, P. Xu, H. Chen, Y. Li, W. Bu, Z. Shu, Y. Li, J. Zhang, L. Zhang, L. Pan, X. Cui, Z. Hua, J. Wang, L. Zhang and J. Shi, *Adv. Mater.*, 2013, **25**, 3100-3105.
23 J. Sun, H. Rijckaert, Y. Maegawa, S. Inagaki, P. Van Der Voort and A. M. Kaczmarek, *Chem. Mater.*, 2022, **34**, 3770-3780.
24 S. Shahbazi, C. J. Oldham, A. D. Mullen, J. D. Auxier Ii and H. L. Hall, *Radiochim. Acta*, 2019, **107**, 1173-1184.
25 A. M. Kaczmarek, R. Van Deun and P. Van Der Voort, *J. Mater. Chem. C*, 2019, **7**, 4222-4229.
26 A. M. Kaczmarek and P. Van Der Voort, *J. Mater. Chem. C*, 2019, **7**, 8109-8119.
27 D. Jiang, X. Yang, H. Chen, F. Wang, S. Wang, T. Zhu, L. Zhang and S. Huang, *Dalton Trans.*, 2019, **48**, 2206-2212.
28 Y.-N. Gu, J.-F. Lu, H. Liu, B. Zhao, X.-H. Zhou, Y.-Q. Zhao, Q.-Z. Sun and B.-G. Zhang, *Cryst. Growth Des.*, 2022, **22**, 4874-4884.
29 W. Liu, A. M. Kaczmarek, P. Van Der Voort and R. Van Deun, *Dalton Trans.*, 2022, **51**, 11467-11475.
30 H. Zuo, Y. Li and Y. Liao, *ACS Appl. Mater. Interfaces*, 2019, **11**, 39201-39208.

